PROCEEDINGS A

rspa.royalsocietypublishing.org

Research

Article submitted to journal

Subject Areas:
mechanical engineering, differential equations

Keywords:
nonlinear dynamics, double Hopf bifurcation, center manifold reduction, machine tool vibration

Author for correspondence:
Tamas G. Molnar
e-mail: molnar@mm.bme.hu

On the analysis of the double Hopf bifurcation in machining processes via center manifold reduction

T. G. Molnar[1], Z. Dombovari[1], T. Insperger[2] and G. Stepan[1]

[1]Department of Applied Mechanics, Budapest University of Technology and Economics, H-1111 Budapest, Hungary

[2]Department of Applied Mechanics, Budapest University of Technology and Economics and MTA-BME Lendület Human Balancing Research Group, H-1111 Budapest, Hungary

The single-degree-of-freedom model of orthogonal cutting is investigated to study machine tool vibrations in the vicinity of a double Hopf bifurcation point. Center manifold reduction and normal form calculations are performed to investigate the long-term dynamics of the cutting process. The normal form of the four-dimensional center subsystem is derived analytically, and the possible topologies in the infinite-dimensional phase space of the system are revealed. It is shown that bistable parameter regions exist where unstable periodic and, in certain cases, unstable quasi-periodic motions coexist with the equilibrium. Taking into account the non-smoothness caused by loss of contact between the tool and the workpiece, the boundary of the bistable region is also derived analytically. The results are verified by numerical continuation. The possibility of (transient) chaotic motions in the global non-smooth dynamics is shown.

1. Introduction

Improving the productivity of metal cutting operations is highly important for the manufacturing society. The occurrence of harmful vibrations during machining – known as machine tool chatter – limits the achievable productivity. Therefore, studying the dynamics of machine tool chatter is an active field of research.

THE ROYAL SOCIETY PUBLISHING

The aim of analysing machine tool vibrations is to identify those regions in the space of the technological parameters, which are associated with chatter-free manufacturing processes. These parameter regions are typically illustrated in the plane of the spindle speed and the depth of cut; this picture is called stability lobe diagram or stability chart. The first successful efforts to describe chatter and to derive stability charts are presented in the works of Tobias [1] and Tlusty [2].

Machine tool vibrations are described by delay-differential equations (DDEs), since the chip thickness, which determines the cutting force, is affected both by actual and delayed tool positions due to the surface regeneration effect. Since DDEs have infinite-dimensional phase space representation [3], the dynamics of machine tool chatter is rich and intricate. Furthermore, the modelling DDEs are typically nonlinear, since the cutting force is a nonlinear function of the chip thickness [4].

Here, we restrict ourselves to the analysis of autonomous DDEs, which are the typical models of turning operations. Along the stability boundaries (or stability lobes) of turning, Hopf bifurcation occurs, which gives rise to a periodic solution of the nonlinear system. This periodic solution plays an important role in determining the global dynamics of the cutting process that may involve the high frequency self-excited vibration called chatter. The effect of nonlinearities on the occurrence of machine tool chatter was investigated for example in [5–8], whereas the bifurcation analysis of machining processes can be found in [9–14] for turning and in [15] for milling operations. The theory of Hopf bifurcation in DDEs is covered by [3,16–19]. The most popular approaches for bifurcation analysis are the rigorous center manifold reduction [20] and the method of multiple scales [12,13]. Note that other methods also exist for the computation of periodic solutions [21], e.g. the method of small parameters or the theory of averaging [5,22–26].

In this paper, we analyse the intersection of stability boundaries where double Hopf bifurcation takes place. The double Hopf bifurcation complicates the dynamics of metal cutting by giving rise to a quasi-periodic solution [27]. Examples for the analysis of double Hopf bifurcation can be found in [28–38] for various dynamical systems. The double Hopf bifurcation in metal cutting was analysed in [39] using the method of multiple scales. Now we extend this work by analysing a slightly different model using center manifold reduction. In particular, we investigate the possible topologies in the phase portraits of the system near the double Hopf bifurcation and we also discuss the phenomenon of bistability. We verify the results by numerical continuation. Continuation of periodic solutions of nonlinear DDEs can be carried out by the software DDE-BIFTOOL [40], whereas the arising quasi-periodic solution can be computed by the software KNUT [41,42] or by the algorithm used in [15]. In this paper, we use the latter algorithm to verify the results of center manifold reduction.

The rest of the paper is organised as follows. Section 2 presents the mechanical model of turning. Section 3 discusses the linear stability analysis, whereas Sec. 4 shows the bifurcation analysis using center manifold reduction. The resulting stability charts and bifurcation diagrams are presented together with implications on the global dynamic behaviour in Sec. 5. Conclusions are drawn in Sec. 6.

2. Equation of Motion

We consider the single-degree-of-freedom model of orthogonal cutting shown in Fig. 1(a). The equation of motion for the tool can be given in dimensionless form as follows (see [11] for details):

$$x''(t) + 2\zeta x'(t) + x(t) = w\Big((x(t-\tau) - x(t)) + \eta_2 \left(x(t-\tau) - x(t)\right)^2 + \eta_3 \left(x(t-\tau) - x(t)\right)^3 \Big), \tag{2.1}$$

where t is the dimensionless time measured by the time period of the free undamped natural oscillation of the system, x indicates the dimensionless position of the tool with respect to the constant theoretical chip thickness set to have unit length in Fig. 1, and ζ is the damping ratio of the dominant vibration mode of the system. The right-hand side of Eq. (2.1) is proportional to the variation of the dimensionless, x-directional cutting force component, which is assumed to be a cubic polynomial function of the dimensionless chip thickness variation $x(t-\tau) - x(t)$.

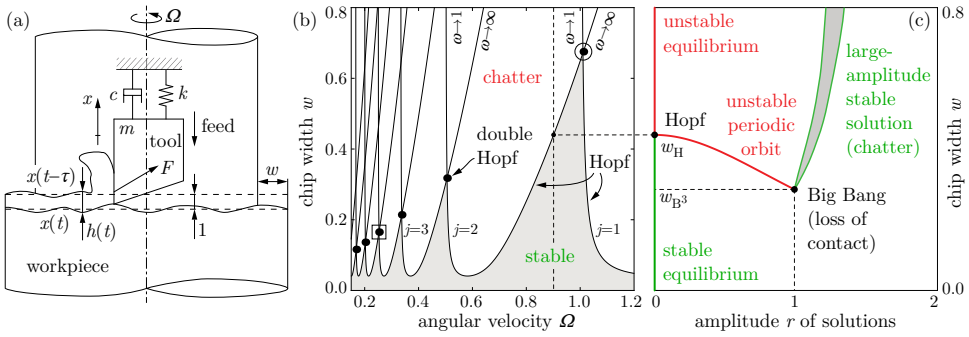

Figure 1. Single-degree-of-freedom mechanical model of orthogonal cutting (a); stability lobe diagram of the cutting process (b); a typical bifurcation scenario (c).

Parameter τ is the dimensionless regenerative delay or, equivalently, the period of workpiece rotation related to the dimensionless angular velocity Ω of the workpiece: $\tau = 2\pi/\Omega$. Parameter w is the dimensionless chip width, whereas η_2 and η_3 denote dimensionless quadratic and cubic cutting-force coefficients related to the prescribed feed per revolution, which is just the unit theoretical chip thickness.

Equation (2.1) is a delay-differential equation with cubic nonlinearity. The cubic cutting force model was introduced in [5]. Note that other cutting force characteristics also exist, see [4] and the references therein, but these characteristics can also be approximated by cubic polynomials using Taylor series expansion. Approximation of the nonlinearity by a cubic expression is a necessary step for the subsequent bifurcation analysis in Sec. 4 and Sec. 5.

Equation (2.1) is valid only for positive dimensionless chip thickness, $h(t) = 1 + x(t-\tau) - x(t) > 0$. For large-amplitude vibrations, it might occur that the dimensionless chip thickness $h(t)$ drops to zero or to negative values, which indicates that the tool gets out of the workpiece and loses contact with the material. In such cases, the cutting force on the right-hand side of (2.1) becomes zero irrespective of the tool's position. At this point, we do not investigate loss of contact between the tool and the workpiece and assume that $h(t) > 0$ and (2.1) is valid during the entire cutting process.

In the rest of the paper, we deal with the stability and bifurcation analysis of (2.1). For convenience, the equation is transformed into the first-order form

$$\mathbf{y}'(t) = \mathbf{L}\mathbf{y}(t) + \mathbf{R}\mathbf{y}(t-\tau) + \mathbf{g}(\mathbf{y}_t)\,, \tag{2.2}$$

where $\mathbf{y}$ is the vector of state variables, $\mathbf{L}$ and $\mathbf{R}$ are the coefficient matrices of the linear and the retarded terms, respectively, and $\mathbf{g}$ contains all nonlinear terms:

$$\begin{aligned} \mathbf{y}(t) &= \begin{bmatrix} x(t) \\ x'(t) \end{bmatrix}, \quad \mathbf{L} = \begin{bmatrix} 0 & 1 \\ -(1+w) & -2\zeta \end{bmatrix}, \quad \mathbf{R} = \begin{bmatrix} 0 & 0 \\ w & 0 \end{bmatrix}, \\ \mathbf{g}(\mathbf{y}_t) &= \begin{bmatrix} 0 \\ w\left(\eta_2 \left(y_1(t-\tau) - y_1(t)\right)^2 + \eta_3 \left(y_1(t-\tau) - y_1(t)\right)^3\right) \end{bmatrix}. \end{aligned} \tag{2.3}$$

Here subscript 1 refers to the first component of a vector, i.e., $y_1(t) = x(t)$.

Since delay-differential equations have infinite-dimensional phase space [3], the state of the system is not determined solely by the vector $\mathbf{y}(t)$. Instead, we use a function defined in the Banach space $\mathcal{B}$ of continuously differentiable vector-valued functions to describe the evolution of the system: we introduce the shift $\mathbf{y}_t \in \mathcal{B} : [-\tau, 0] \to \mathbb{R}^2$, $\mathbf{y}_t(\theta) = \mathbf{y}(t+\theta)$. Using $\mathbf{y}_t$, system (2.1) can be represented in operator differential equation (OpDE) form as

$$\mathbf{y}_t' = \mathcal{A}\mathbf{y}_t + \mathcal{F}(\mathbf{y}_t)\,, \tag{2.4}$$

where $\mathcal{A}, \mathcal{F} : \mathcal{B} \to \mathcal{B}$ are the linear and the nonlinear operators, respectively, defined by

$$(\mathcal{A}\mathbf{u})(\theta) = \begin{cases} \frac{\mathrm{d}}{\mathrm{d}\theta}\mathbf{u}(\theta) & \text{if } \theta \in [-\tau, 0)\,, \\ \mathbf{L}\mathbf{u}(0) + \mathbf{R}\mathbf{u}(-\tau) & \text{if } \theta = 0\,, \end{cases} \tag{2.5}$$

$$(\mathcal{F}(\mathbf{u}))(\theta) = \begin{cases} \mathbf{0} & \text{if } \theta \in [-\tau, 0)\,, \\ \mathbf{g}(\mathbf{u}) & \text{if } \theta = 0\,. \end{cases} \tag{2.6}$$

3. Linear Stability Analysis

Equation (2.1) has a single equilibrium $x(t) \equiv 0$, which corresponds to stationary cutting. Machine tool chatter is associated with the loss of stability of this equilibrium. Substitution of the exponential trial solution $x(t) = C\mathrm{e}^{\lambda t}$, $\lambda, C \in \mathbb{C}$ into (2.1) gives the characteristic function

$$D(\lambda) := \det\left(\lambda\mathbf{I} - \mathbf{L} - \mathbf{R}\mathrm{e}^{-\lambda\tau}\right) = \lambda^2 + 2\zeta\lambda + 1 + w\left(1 - \mathrm{e}^{-\lambda\tau}\right)\,. \tag{3.1}$$

Its infinitely many zeros – known as characteristic exponents – are the same as the eigenvalues of the operator $\mathcal{A}$ in (2.5). The trivial solution is exponentially asymptotically stable if and only if all the characteristic exponents lie in the open left half of the complex plane. The system is at the boundary of stability if a single real root $\lambda = 0$ or a pair of complex conjugate roots $\lambda = \pm\mathrm{i}\omega$ ($\mathrm{i}^2 = -1$, $\omega > 0$) exists, while no characteristic exponents have positive real part. For (3.1), only the latter case with critical roots $\lambda = \pm\mathrm{i}\omega$ is possible, which corresponds to a Hopf bifurcation in the nonlinear system. The analysis of the Hopf bifurcation can be found in [9–11] in details. The Hopf bifurcation points can be located after the separation of $D(\pm\mathrm{i}\omega) = 0$ into real and imaginary parts:

$$\begin{aligned} R(\omega) =& -\omega^2 + 1 + w\left(1 - \cos(\omega\tau)\right)\,, \\ S(\omega) =& 2\zeta\omega + w\sin(\omega\tau)\,. \end{aligned} \tag{3.2}$$

Solving $R(\omega) = 0$ and $S(\omega) = 0$ gives the linear stability boundaries in the form

$$w_{\mathrm{H}}(\omega) = \frac{\left(\omega^2 - 1\right)^2 + 4\zeta^2\omega^2}{2\left(\omega^2 - 1\right)}\,,\quad \tau_{\mathrm{H}}(j,\omega) = \frac{2}{\omega}\left(j\pi - \arctan\left(\frac{\omega^2 - 1}{2\zeta\omega}\right)\right)\,,\quad \Omega_{\mathrm{H}}(j,\omega) = \frac{2\pi}{\tau_{\mathrm{H}}(j,\omega)}\,, \tag{3.3}$$

where subscript H indicates that (3.3) gives the location of Hopf bifurcation. Note that (3.3) defines a family of curves called stability lobes where $j \in \mathbb{Z}^+$ is the lobe number. Depicting the stability boundaries in the plane (Ω, w) of the technological parameters leads to so-called stability lobe diagrams (see the example in Fig. 1(b) for $\zeta = 0.02$ where gray shading indicates the linearly stable region associated with chatter-free cutting process).

As it was shown in [9–11], subcritical Hopf bifurcation occurs along the stability lobes. In the vicinity of the stability boundaries, the bifurcation gives rise to an unstable periodic orbit around the linearly stable equilibrium with approximate period $2\pi/\omega$. At the intersection points of the stability lobes, a codimension two bifurcation – often referred to as double Hopf bifurcation – takes place. At these points, two pairs of characteristic exponents $\lambda = \pm\mathrm{i}\omega_{1,2}$ lie on the imaginary axis ($\omega_{1,2} > 0$). Let us consider the intersection of the lobes with lobe numbers j_1 and j_2. The location of this point (the so-called double Hopf point) is given by $w_{\mathrm{HH}} := w_{\mathrm{H}}(\omega_1) = w_{\mathrm{H}}(\omega_2)$, $\tau_{\mathrm{HH}} := \tau_{\mathrm{H}}(j_1, \omega_1) = \tau_{\mathrm{H}}(j_2, \omega_2)$ and $\Omega_{\mathrm{HH}} := \Omega_{\mathrm{H}}(j_1, \omega_1) = \Omega_{\mathrm{H}}(j_2, \omega_2)$, which can be obtained by solving $R(\omega_1) = 0$, $S(\omega_1) = 0$, $R(\omega_2) = 0$ and $S(\omega_2) = 0$ numerically for ω_1, ω_2, w and τ. Subscript HH refers to Hopf-Hopf (double Hopf) bifurcation.

The rest of the paper deals with the analysis of the double Hopf bifurcation via center manifold reduction and the derivation of the normal form of the resulting four-dimensional center subsystem.

4. Center Manifold Reduction and Normal Form Calculations

In this section, center manifold reduction is used to analyse the long-term dynamics of the time-delay system (2.1) in the vicinity of the double Hopf bifurcation point. The theory of center manifold reduction is discussed in [3]. The calculation follows the steps of the single Hopf bifurcation analysis, which is described in [9–11] in details.

At a double Hopf point on the boundary of the linearly stable region, the system has four characteristic exponents located on the imaginary axis, while all the other characteristic roots are located in the open left half-plane. Therefore, the long-term dynamics of the system is determined by the flow on a four-dimensional center manifold, which is embedded in the infinite-dimensional phase space of (2.1). This flow can be analysed by decomposing the four-dimensional center subsystem (see (4.24) at the end of this Section). In what follows, we perform this decomposition using the theorem given by (3.10) and (3.11) in Chap. 7 of [3].

The decomposition theorem of [3] introduces the operator $\mathcal{A}^*$, which is formally adjoint to operator $\mathcal{A}$ relative to a certain bilinear form. The formal adjoint $\mathcal{A}^*:\mathcal{B}^*\to\mathcal{B}^*$ must satisfy $(\mathbf{v},\mathcal{A}\mathbf{u})=(\mathcal{A}^*\mathbf{v},\mathbf{u})$ for any pair of $\mathbf{u}\in\mathcal{B}:[-\tau,0]\to\mathbb{R}^2$ and $\mathbf{v}\in\mathcal{B}^*:[0,\tau]\to\mathbb{R}^2$, where $\mathcal{B}^*$ is the adjoint space and operation $(\ ,\ ):\mathcal{B}^*\times\mathcal{B}\to\mathbb{R}$ indicates the bilinear form. The definition of the formal adjoint and the bilinear form can be found in [3] (see (3.1) and (3.3) in Chap. 7), and here they become

$$\left(\mathcal{A}^*\mathbf{v}\right)(\varphi)=\begin{cases}-\dfrac{\mathrm{d}}{\mathrm{d}\varphi}\mathbf{v}(\varphi) & \text{if } \varphi\in(0,\tau]\,,\\ \mathbf{L}^*\mathbf{v}(0)+\mathbf{R}^*\mathbf{v}(\tau) & \text{if } \varphi=0\,,\end{cases} \tag{4.1}$$

$$(\mathbf{u},\mathbf{v})=\mathbf{u}^*(0)\mathbf{v}(0)+\int_0^\tau \mathbf{u}^*(\varphi)\mathbf{R}\mathbf{v}(\varphi-\tau)\mathrm{d}\varphi\,, \tag{4.2}$$

where the superscript $*$ of $\mathbf{R}$, $\mathbf{L}$ and $\mathbf{u}$ refers to conjugate transpose.

(a) Right and Left Eigenvectors

The four-dimensional center subspace of the associated linear system is tangent to the plane spanned by those infinite-dimensional right eigenvectors (eigenfunctions) of operator $\mathcal{A}$, which correspond to the four critical characteristic exponents $\lambda=\pm i\omega_k$, $k=1,2$. From this point on, index $k=1,2$ is used to indicate that an expression is related to one of the angular frequencies, i.e., either to ω_1 or to ω_2. For $\tau=\tau_{\mathrm{HH}}$ and $w=w_{\mathrm{HH}}$, the four eigenvectors $\mathbf{s}_k(\theta)$ and $\bar{\mathbf{s}}_k(\theta)$ satisfy

$$\left(\mathcal{A}\mathbf{s}_k\right)(\theta)=\mathrm{i}\omega_k\mathbf{s}_k(\theta)\,,\quad \left(\mathcal{A}\bar{\mathbf{s}}_k\right)(\theta)=-\mathrm{i}\omega_k\bar{\mathbf{s}}_k(\theta)\,, \tag{4.3}$$

where overbar indicates complex conjugate. Decomposing the eigenvectors into real and imaginary parts as $\mathbf{s}_k(\theta)=\mathbf{s}_{k,\mathrm{R}}(\theta)+\mathrm{i}\mathbf{s}_{k,\mathrm{I}}(\theta)$, substituting $\tau=\tau_{\mathrm{HH}}$, $w=w_{\mathrm{HH}}$ and the definition (2.5) of operator $\mathcal{A}$, we get the boundary value problem

$$\frac{\mathrm{d}}{\mathrm{d}\theta}\mathbf{s}(\theta)=\mathbf{B}_{8\times8}\mathbf{s}(\theta)\,,\quad \theta\in[-\tau_{\mathrm{HH}},0)\,, \tag{4.4}$$

$$\mathbf{L}_{8\times8}\mathbf{s}(0)+\mathbf{R}_{8\times8}\mathbf{s}(-\tau_{\mathrm{HH}})=\mathbf{B}_{8\times8}\mathbf{s}(0)\,. \tag{4.5}$$

The coefficient matrices and $\mathbf{s}(\theta)$ are defined as

$$\mathbf{s}(\theta)=\begin{bmatrix}\mathbf{s}_{1,\mathrm{R}}(\theta)\\ \mathbf{s}_{1,\mathrm{I}}(\theta)\\ \mathbf{s}_{2,\mathrm{R}}(\theta)\\ \mathbf{s}_{2,\mathrm{I}}(\theta)\end{bmatrix},\quad \mathbf{B}_{8\times8}=\begin{bmatrix}\mathbf{0} & -\omega_1\mathbf{I} & \mathbf{0} & \mathbf{0}\\ \omega_1\mathbf{I} & \mathbf{0} & \mathbf{0} & \mathbf{0}\\ \mathbf{0} & \mathbf{0} & \mathbf{0} & -\omega_2\mathbf{I}\\ \mathbf{0} & \mathbf{0} & \omega_2\mathbf{I} & \mathbf{0}\end{bmatrix}, \tag{4.6}$$

$$\mathbf{L}_{8\times8}=\mathrm{diag}\left[\mathbf{L},\mathbf{L},\mathbf{L},\mathbf{L}\right]\big|_{w=w_{\mathrm{HH}}}\,,\quad \mathbf{R}_{8\times8}=\mathrm{diag}\left[\mathbf{R},\mathbf{R},\mathbf{R},\mathbf{R}\right]\big|_{w=w_{\mathrm{HH}}}\,,$$

where $\mathbf{I}$ and $\mathbf{0}$ denote the 2×2 identity and zero matrices, respectively, and diag refers to block-diagonal matrices. The solution of (4.4) can be written in exponential form as $\mathbf{s}(\theta)=\mathrm{e}^{\mathbf{B}_{8\times8}\theta}\mathbf{c}$. The

constant **c** can be determined from (4.5). In order to select the norm of the right eigenvectors, four components of **c** can be chosen arbitrarily. Now we choose $c_1 = 1$, $c_3 = 0$, $c_5 = 1$, and $c_7 = 0$, whence we get

$$\mathbf{s}_{k,\mathrm{R}}(\theta) = \begin{bmatrix} \cos(\omega_k\theta) \\ -\omega_k \sin(\omega_k\theta) \end{bmatrix}, \quad \mathbf{s}_{k,\mathrm{I}}(\theta) = \begin{bmatrix} \sin(\omega_k\theta) \\ \omega_k \cos(\omega_k\theta) \end{bmatrix}. \tag{4.7}$$

The decomposition theorem of [3] also uses the so-called left eigenvectors: the eigenvectors $\mathbf{n}_k(\varphi)$ and $\overline{\mathbf{n}}_k(\varphi)$ of the adjoint operator $\mathcal{A}^*$. Since the eigenvalues of $\mathcal{A}^*$ are complex conjugates to those of $\mathcal{A}$, the left eigenvectors $\mathbf{n}_k(\varphi)$ and $\overline{\mathbf{n}}_k(\varphi)$ satisfy

$$\left(\mathcal{A}^*\mathbf{n}_k\right)(\varphi) = -\mathrm{i}\omega_k\mathbf{n}_k(\varphi), \quad \left(\mathcal{A}^*\overline{\mathbf{n}}_k\right)(\varphi) = \mathrm{i}\omega_k\overline{\mathbf{n}}_k(\varphi) \tag{4.8}$$

for $\tau = \tau_{\mathrm{HH}}$ and $w = w_{\mathrm{HH}}$. We decompose the eigenvectors into real and imaginary parts as $\mathbf{n}_k(\varphi) = \mathbf{n}_{k,\mathrm{R}}(\varphi) + \mathrm{i}\mathbf{n}_{k,\mathrm{I}}(\varphi)$, where $\mathbf{n}_{k,\mathrm{R}}(\varphi)$ and $\mathbf{n}_{k,\mathrm{I}}(\varphi)$ can be obtained from the boundary value problem defined by (4.8) and (4.1) in the same way as we computed $\mathbf{s}_{k,\mathrm{R}}(\theta)$ and $\mathbf{s}_{k,\mathrm{I}}(\theta)$. The norm of the left eigenvectors cannot be selected arbitrarily, since they must satisfy the following orthonormality condition in order to apply the decomposition theorem of [3]:

$$(\mathbf{n}_{1,\mathrm{R}}, \mathbf{s}_{1,\mathrm{R}}) = 1, \quad (\mathbf{n}_{1,\mathrm{R}}, \mathbf{s}_{1,\mathrm{I}}) = 0, \quad (\mathbf{n}_{2,\mathrm{R}}, \mathbf{s}_{2,\mathrm{R}}) = 1, \quad (\mathbf{n}_{2,\mathrm{R}}, \mathbf{s}_{2,\mathrm{I}}) = 0. \tag{4.9}$$

Solving the boundary value problem (4.8) constrained by the orthonormality condition (4.9), we get the left eigenfunctions in the form

$$\begin{aligned} \mathbf{n}_{k,\mathrm{R}}(\varphi) &= \frac{2}{p_k^2+q_k^2}\begin{bmatrix} (2\zeta p_k + \omega_k q_k)\cos(\omega_k\varphi) + (\omega_k p_k - 2\zeta q_k)\sin(\omega_k\varphi) \\ p_k\cos(\omega_k\varphi) - q_k\sin(\omega_k\varphi) \end{bmatrix}, \\ \mathbf{n}_{k,\mathrm{I}}(\varphi) &= \frac{2}{p_k^2+q_k^2}\begin{bmatrix} (-\omega_k p_k + 2\zeta q_k)\cos(\omega_k\varphi) + (2\zeta p_k + \omega_k q_k)\sin(\omega_k\varphi) \\ q_k\cos(\omega_k\varphi) + p_k\sin(\omega_k\varphi) \end{bmatrix}, \end{aligned} \tag{4.10}$$

where the constants p_k and q_k read

$$p_k = 2\zeta + \tau_{\mathrm{HH}}\left(1 + w_{\mathrm{HH}} - \omega_k^2\right), \quad q_k = 2\omega_k\left(1 + \zeta\tau_{\mathrm{HH}}\right). \tag{4.11}$$

(b) Decomposition of the Solution Space

Using the right and left eigenvectors, the four-dimensional center subspace can now be separated via the decomposition theorem given by (3.10) and (3.11) in Chap. 7 of [3]. We decompose the solution as

$$\mathbf{y}_t(\theta) = z_1(t)\mathbf{s}_{1,\mathrm{R}}(\theta) + z_2(t)\mathbf{s}_{1,\mathrm{I}}(\theta) + z_3(t)\mathbf{s}_{2,\mathrm{R}}(\theta) + z_4(t)\mathbf{s}_{2,\mathrm{I}}(\theta) + \mathbf{y}_{t\mathrm{n}}(\theta), \tag{4.12}$$

where $z_1(t)$, $z_2(t)$, $z_3(t)$ and $z_4(t)$ are local coordinates on the attractive center manifold, which describe the long-term dynamics of the time-delay system (2.1), whereas $\mathbf{y}_{t\mathrm{n}}(\theta)$ accounts for the remaining infinite-dimensional stable subsystem with coordinates transverse to the center manifold. The decomposition theorem gives the formula of these components:

$$\begin{aligned} &z_1(t) = (\mathbf{n}_{1,\mathrm{R}}, \mathbf{y}_t), \quad z_2(t) = (\mathbf{n}_{1,\mathrm{I}}, \mathbf{y}_t), \quad z_3(t) = (\mathbf{n}_{2,\mathrm{R}}, \mathbf{y}_t), \quad z_4(t) = (\mathbf{n}_{2,\mathrm{I}}, \mathbf{y}_t), \\ &\mathbf{y}_{t\mathrm{n}}(\theta) = \mathbf{y}_t(\theta) - z_1(t)\mathbf{s}_{1,\mathrm{R}}(\theta) - z_2(t)\mathbf{s}_{1,\mathrm{I}}(\theta) - z_3(t)\mathbf{s}_{2,\mathrm{R}}(\theta) - z_4(t)\mathbf{s}_{2,\mathrm{I}}(\theta). \end{aligned} \tag{4.13}$$

From this point on, we omit the argument t from z_1, z_2, z_3 and z_4 for the sake of simplicity. Differentiating (4.13) with respect to time and using (2.4), (4.12) and (4.3), we get

$$\begin{bmatrix} z_1' \\ z_2' \\ z_3' \\ z_4' \\ \mathbf{y}_{t\mathrm{n}}' \end{bmatrix} = \begin{bmatrix} 0 & \omega_1 & 0 & 0 & \mathcal{O} \\ -\omega_1 & 0 & 0 & 0 & \mathcal{O} \\ 0 & 0 & 0 & \omega_2 & \mathcal{O} \\ 0 & 0 & -\omega_2 & 0 & \mathcal{O} \\ \mathbf{0} & \mathbf{0} & \mathbf{0} & \mathbf{0} & \mathcal{A} \end{bmatrix} \begin{bmatrix} z_1 \\ z_2 \\ z_3 \\ z_4 \\ \mathbf{y}_{t\mathrm{n}} \end{bmatrix} + \begin{bmatrix} n_{1,\mathrm{R},2}(0)\mathcal{F}_2(0) \\ n_{1,\mathrm{I},2}(0)\mathcal{F}_2(0) \\ n_{2,\mathrm{R},2}(0)\mathcal{F}_2(0) \\ n_{2,\mathrm{I},2}(0)\mathcal{F}_2(0) \\ \mathcal{G}(\mathbf{y}_t) \end{bmatrix}, \tag{4.14}$$

$$\mathcal{G}(\mathbf{y}_t) = \mathcal{F}(\mathbf{y}_t) - \mathcal{F}_2(0)\left(n_{1,\mathrm{R},2}(0)\mathbf{s}_{1,\mathrm{R}} + n_{1,\mathrm{I},2}(0)\mathbf{s}_{1,\mathrm{I}} + n_{2,\mathrm{R},2}(0)\mathbf{s}_{2,\mathrm{R}} + n_{2,\mathrm{I},2}(0)\mathbf{s}_{2,\mathrm{I}}\right),$$

where $\mathfrak{o}:\mathbb{R}\to\mathcal{B}$ is a zero operator, $\mathcal{O}:\mathcal{B}\to\mathbb{R}$ is a zero functional, subscript 2 in $n_{k,\mathrm{R},2}$ and $n_{k,\mathrm{I},2}$ indicates the second component of vectors, and $\mathcal{F}_2(0)$ shortly indicates the second component of $\mathcal{F}(\mathbf{y}_t)$ at $\theta=0$ with $\tau=\tau_{\mathrm{HH}}$ and $w=w_{\mathrm{HH}}$.

(c) Approximation of the Center Manifold

Equation (4.14) shows that the four-dimensional center subsystem is decoupled in the associated linear system, but there is still coupling in the nonlinear terms. In order to fully decouple the four-dimensional subsystem, the dynamics must be restricted to the center manifold of form $\mathbf{y}_{tn}=\mathbf{y}_{tn}^{\mathrm{CM}}(z_1,z_2,z_3,z_4)$. The nonlinear terms in the first four rows of (4.14) must be expanded into Taylor series in terms of z_1, z_2, z_3 and z_4 in order to do normal form analysis – we must expand $\mathcal{F}_2(0)$ up to third order. The computation of the center manifold and the Taylor expansion is rather lengthy, but it can be tackled by symbolic algebra. Now we present the milestones of this process.

Substituting the decomposed solution (4.12) into the definition (2.6) of $\mathcal{F}$, we get the Taylor series expansion of $\mathcal{F}_2(0)$ if the center manifold $\mathbf{y}_{tn}=\mathbf{y}_{tn}^{\mathrm{CM}}(z_1,z_2,z_3,z_4)$ is expanded into Taylor series in terms of $z_{1,2,3,4}$. The second-order terms in $\mathcal{F}_2(0)$ are independent of $\mathbf{y}_{tn}^{\mathrm{CM}}$, the expansion of the center manifold is necessary only to obtain the cubic (and higher-order) terms in $\mathcal{F}_2(0)$. The quadratic part of $\mathcal{F}_2(0)$ is of form

$$\begin{aligned}\mathcal{F}_2^{\mathrm{2nd}}(0)=&F_{11}z_1^2+F_{22}z_2^2+F_{33}z_3^2+F_{44}z_4^2\\&+F_{12}z_1z_2+F_{13}z_1z_3+F_{14}z_1z_4+F_{23}z_2z_3+F_{24}z_2z_4+F_{34}z_3z_4\,,\\F_{mn}=&\frac{1}{2}\left.\frac{\partial^2\mathcal{F}_2(0)}{\partial z_m^2}\right|_{\mathbf{0}},\quad\text{if } m=n\,,\quad F_{mn}=\left.\frac{\partial^2\mathcal{F}_2(0)}{\partial z_m\partial z_n}\right|_{\mathbf{0}},\ \text{if } m<n\,,\end{aligned}\tag{4.15}$$

$m,n=1,2,3,4$, where the subscript $\mathbf{0}$ stands for the substitution $\mathbf{y}_t(0)=\mathbf{0}$. In order to include all cubic terms in $\mathcal{F}_2(0)$, we need at least the second-order expansion of the center manifold $\mathbf{y}_{tn}^{\mathrm{CM}}$ in terms of $z_{1,2,3,4}$:

$$\begin{aligned}\mathbf{y}_{tn}^{\mathrm{CM}}(z_1,z_2,z_3,z_4)(\theta)\approx\frac{1}{2}\Big(&\mathbf{h}_{11}(\theta)z_1^2+\mathbf{h}_{22}(\theta)z_2^2+\mathbf{h}_{33}(\theta)z_3^2+\mathbf{h}_{44}(\theta)z_4^2\\&+2\mathbf{h}_{12}(\theta)z_1z_2+2\mathbf{h}_{13}(\theta)z_1z_3+2\mathbf{h}_{14}(\theta)z_1z_4+2\mathbf{h}_{23}(\theta)z_2z_3+2\mathbf{h}_{24}(\theta)z_2z_4+2\mathbf{h}_{34}(\theta)z_3z_4\Big)\,.\end{aligned}\tag{4.16}$$

The coefficients $\mathbf{h}_{mn}(\theta)$ $(m,n=1,2,3,4,\ m\le n)$ can be determined as follows. Both sides of (4.16) are differentiated with respect to time, then the first four rows of (4.14) are substituted into the right-hand side and the fifth row of (4.14) is substituted into the left-hand side. The case $\theta\in[-\tau_{\mathrm{HH}},0)$ is considered and the definitions (2.5)-(2.6) of $\mathcal{A}$ and $\mathcal{F}$ are substituted accordingly. Afterwards, the derivative of (4.16) with respect to θ is substituted and the second-order approximation $\mathcal{F}_2(0)\approx\mathcal{F}_2^{\mathrm{2nd}}(0)$ is used. Finally, the coefficients of the quadratic terms of $z_{1,2,3,4}$ are collected and a polynomial balance is considered. This leads to three decoupled sets of non-homogeneous first-order differential equations:

$$\frac{\mathrm{d}}{\mathrm{d}\theta}\mathbf{H}_l(\theta)=\mathbf{C}_l\mathbf{H}_l(\theta)+\mathbf{p}_{1,l}\cos(\omega_1\theta)+\mathbf{q}_{1,l}\sin(\omega_1\theta)+\mathbf{p}_{2,l}\cos(\omega_2\theta)+\mathbf{q}_{2,l}\sin(\omega_2\theta)\,,\tag{4.17}$$

$l=1,2,3$, where

$$\mathbf{H}_1(\theta)=\begin{bmatrix}\mathbf{h}_{11}(\theta)\\ \mathbf{h}_{12}(\theta)\\ \mathbf{h}_{22}(\theta)\end{bmatrix},\ \mathbf{H}_2(\theta)=\begin{bmatrix}\mathbf{h}_{33}(\theta)\\ \mathbf{h}_{34}(\theta)\\ \mathbf{h}_{44}(\theta)\end{bmatrix},\ \mathbf{H}_3(\theta)=\begin{bmatrix}\mathbf{h}_{13}(\theta)\\ \mathbf{h}_{14}(\theta)\\ \mathbf{h}_{23}(\theta)\\ \mathbf{h}_{24}(\theta)\end{bmatrix},\quad \mathbf{Q}_k=\frac{2}{p_k^2+q_k^2}\begin{bmatrix}p_k & q_k\\ q_k\omega_k & -p_k\omega_k\end{bmatrix},$$

$$\begin{bmatrix}\mathbf{p}_{k,1} & \mathbf{q}_{k,1}\end{bmatrix}=\begin{bmatrix}2F_{11}\mathbf{Q}_k\\ F_{12}\mathbf{Q}_k\\ 2F_{22}\mathbf{Q}_k\end{bmatrix},\quad \begin{bmatrix}\mathbf{p}_{k,2} & \mathbf{q}_{k,2}\end{bmatrix}=\begin{bmatrix}2F_{33}\mathbf{Q}_k\\ F_{34}\mathbf{Q}_k\\ 2F_{44}\mathbf{Q}_k\end{bmatrix},\quad \begin{bmatrix}\mathbf{p}_{k,3} & \mathbf{q}_{k,3}\end{bmatrix}=\begin{bmatrix}F_{13}\mathbf{Q}_k\\ F_{14}\mathbf{Q}_k\\ F_{23}\mathbf{Q}_k\\ F_{24}\mathbf{Q}_k\end{bmatrix},$$

$$\mathbf{C}_k=\begin{bmatrix}\mathbf{0} & -2\omega_k\mathbf{I} & \mathbf{0}\\ \omega_k\mathbf{I} & \mathbf{0} & -\omega_k\mathbf{I}\\ \mathbf{0} & 2\omega_k\mathbf{I} & \mathbf{0}\end{bmatrix},\quad \mathbf{C}_3=\begin{bmatrix}\mathbf{0} & -\omega_2\mathbf{I} & -\omega_1\mathbf{I} & \mathbf{0}\\ \omega_2\mathbf{I} & \mathbf{0} & \mathbf{0} & -\omega_1\mathbf{I}\\ \omega_1\mathbf{I} & \mathbf{0} & \mathbf{0} & -\omega_2\mathbf{I}\\ \mathbf{0} & \omega_1\mathbf{I} & \omega_2\mathbf{I} & \mathbf{0}\end{bmatrix}. \tag{4.18}$$

The solution of (4.17) takes the form

$$\mathbf{H}_l(\theta)=\mathrm{e}^{\mathbf{C}_l\theta}\mathbf{K}_l+\mathbf{M}_{1,l}\cos(\omega_1\theta)+\mathbf{N}_{1,l}\sin(\omega_1\theta)+\mathbf{M}_{2,l}\cos(\omega_2\theta)+\mathbf{N}_{2,l}\sin(\omega_2\theta)\,, \tag{4.19}$$

$l=1,2,3$. The coefficients $\mathbf{M}_{k,l}$ and $\mathbf{N}_{k,l}$ can be determined by substituting (4.19) back into (4.17) and considering the harmonic balance of the trigonometric terms, which yields

$$\begin{bmatrix}\mathbf{M}_{k,l}\\ \mathbf{N}_{k,l}\end{bmatrix}=\begin{bmatrix}-\mathbf{C}_l & \omega_k\mathbf{I}\\ -\omega_k\mathbf{I} & -\mathbf{C}_l\end{bmatrix}^{-1}\begin{bmatrix}\mathbf{p}_{k,l}\\ \mathbf{q}_{k,l}\end{bmatrix}. \tag{4.20}$$

In order to determine the coefficient $\mathbf{K}_l$ in (4.19), a boundary condition corresponding to (4.17) must be derived and satisfied. The boundary condition is formulated similarly as the differential equation (4.17). Both sides of (4.16) are differentiated with respect to time, then the first four rows of (4.14) are substituted into the right-hand side and the fifth row of (4.14) is substituted into the left-hand side as before. Now the case $\theta=0$ is considered when using the definitions (2.5)-(2.6) of $\mathcal{A}$ and $\mathcal{F}$. Afterwards, (4.16) is substituted and the second-order approximation $\mathcal{F}_2(0)\approx\mathcal{F}_2^{\mathrm{2nd}}(0)$ is used. The coefficients of the quadratic terms of $z_{1,2,3,4}$ are collected for a polynomial balance and, by taking $\tau=\tau_{\mathrm{HH}}$, $w=w_{\mathrm{HH}}$, it leads to the boundary conditions for (4.17) in the form

$$\mathbf{P}_l\mathbf{H}_l(0)+\mathbf{R}_l\mathbf{H}_l(-\tau_{\mathrm{HH}})=\mathbf{p}_{1,l}+\mathbf{p}_{2,l}+\mathbf{r}_l\,, \tag{4.21}$$

where

$$\begin{aligned}
&\mathbf{L}_k=\mathbf{L}_{6\times6}=\mathrm{diag}\,[\mathbf{L},\mathbf{L},\mathbf{L}]|_{w=w_{\mathrm{HH}}}\,,\quad \mathbf{L}_3=\mathbf{L}_{8\times8}\,,\quad \mathbf{P}_l=\mathbf{L}_l-\mathbf{C}_l\,,\\
&\mathbf{R}_k=\mathbf{R}_{6\times6}=\mathrm{diag}\,[\mathbf{R},\mathbf{R},\mathbf{R}]|_{w=w_{\mathrm{HH}}}\,,\quad \mathbf{R}_3=\mathbf{R}_{8\times8}\,,\\
&\mathbf{r}_1=-\begin{bmatrix}0 & 2F_{11} & 0 & F_{12} & 0 & 2F_{22}\end{bmatrix}^{\mathrm{T}},\\
&\mathbf{r}_2=-\begin{bmatrix}0 & 2F_{33} & 0 & F_{34} & 0 & 2F_{44}\end{bmatrix}^{\mathrm{T}},\\
&\mathbf{r}_3=-\begin{bmatrix}0 & F_{13} & 0 & F_{14} & 0 & F_{23} & 0 & F_{24}\end{bmatrix}^{\mathrm{T}}.
\end{aligned} \tag{4.22}$$

Finally, substituting the trial solution (4.19) into the boundary condition (4.21), we obtain the coefficient $\mathbf{K}_l$. After some simplifications, we can write $\mathbf{K}_l$ in the form

$$\mathbf{K}_l=\left(\mathbf{P}_l+\mathbf{R}_l\mathrm{e}^{-\mathbf{C}_l\tau}\right)^{-1}\mathbf{r}_l\,. \tag{4.23}$$

This way, the solution (4.19) of the above boundary value problem is constructed and the coefficients $\mathbf{h}_{mn}(\theta)$ ($m,n=1,2,3,4$, $m\le n$) are available. The second-order approximation (4.16) of the center manifold is obtained and, with (4.12), it can be used to derive the third-order

expansion of $\mathcal{F}_2(0)$ in terms of $z_{1,2,3,4}$. Thus, the nonlinearity in the first four rows of (4.14) is now expressed in terms of the four local coordinates of the center manifold, and we get a four-dimensional subsystem with cubic nonlinearity in the form

$$\begin{bmatrix} z_1' \\ z_2' \\ z_3' \\ z_4' \end{bmatrix} = \begin{bmatrix} 0 & \omega_1 & 0 & 0 \\ -\omega_1 & 0 & 0 & 0 \\ 0 & 0 & 0 & \omega_2 \\ 0 & 0 & -\omega_2 & 0 \end{bmatrix} \begin{bmatrix} z_1 \\ z_2 \\ z_3 \\ z_4 \end{bmatrix} + \begin{bmatrix} G_1(z_1,z_2,z_3,z_4) \\ G_2(z_1,z_2,z_3,z_4) \\ G_3(z_1,z_2,z_3,z_4) \\ G_4(z_1,z_2,z_3,z_4) \end{bmatrix} . \tag{4.24}$$

The lengthy process of center manifold reduction has been performed in order to decouple the four-dimensional center subsystem (4.24). The advantage of this formulation is that the long-term dynamics of the original infinite-dimensional time-delay system (2.1) can be investigated by analysing the finite-dimensional ordinary differential equation (4.24). Hence, from this point on, the bifurcation theorems and normal forms of ordinary differential equations can be used, which are well-known in the literature [17,19]. In the next section, we use normal form theory to analyse the flow on the center manifold and show the existence of periodic and quasi-periodic motions.

(d) Normal Form Equations

The four-dimensional system (4.24) can be transformed into polar form with two amplitudes r_1, r_2 and two phase angles θ_1, θ_2 as

$$\begin{aligned} r_1' &= \mu_1 r_1 + a_{11} r_1^3 + a_{12} r_1 r_2^2 , \quad \theta_1' = \omega_1 + c_{11} r_1^2 + c_{12} r_2^2 , \\ r_2' &= \mu_2 r_2 + a_{21} r_1^2 r_2 + a_{22} r_2^3 , \quad \theta_2' = \omega_2 + c_{21} r_1^2 + c_{22} r_2^2 . \end{aligned} \tag{4.25}$$

Now we focus on the amplitudes r_1, r_2 only and investigate the existence of periodic and quasi-periodic solutions by giving analytical formulae for coefficients μ_1, μ_2, and a_{11}, a_{12}, a_{21}, a_{22}.

The coefficients μ_1, μ_2 of the linear terms in (4.25) are unfolding parameters that are functions of the bifurcation parameters. The double Hopf bifurcation is a codimension two bifurcation, hence two bifurcation parameters must be selected. Now we choose the dimensionless chip width w and the dimensionless angular velocity Ω. For convenience, we introduce the shifted parameters $\hat{w} = w - w_{\mathrm{HH}}$ and $\hat{\Omega} = \Omega - \Omega_{\mathrm{HH}}$ to investigate the system in the vicinity of the double Hopf bifurcation. We can approximate the unfolding parameters by linear functions of the bifurcation parameters as

$$\begin{aligned} \mu_1 &= \gamma_{11} \hat{w} + \gamma_{12} \hat{\Omega} , \\ \mu_2 &= \gamma_{21} \hat{w} + \gamma_{22} \hat{\Omega} , \end{aligned} \tag{4.26}$$

where the constants γ_{mn} $(m,n = 1,2)$ are called the root tendencies. The constants γ_{mn} represent the speed by which the four critical characteristic exponents cross the imaginary axis during the double Hopf bifurcation. They can be obtained via implicit differentiation of the characteristic equation $D(\lambda) = 0$. Using (3.1), this yields

$$\begin{aligned} \gamma_{k1} &= \mathrm{Re}\left(\frac{\partial \lambda}{\partial w}\bigg|_{\lambda = \mathrm{i}\omega_k} \right) = \mathrm{Re}\left(- \frac{\frac{\partial D}{\partial w}}{\frac{\partial D}{\partial \lambda}}\bigg|_{\lambda = \mathrm{i}\omega_k} \right) = \frac{p_k V_k + q_k W_k}{p_k^2 + q_k^2} , \\ \gamma_{k2} &= \mathrm{Re}\left(\frac{\partial \lambda}{\partial \Omega}\bigg|_{\lambda = \mathrm{i}\omega_k} \right) = \mathrm{Re}\left(- \frac{\frac{\partial D}{\partial \tau}\frac{\mathrm{d}\tau}{\mathrm{d}\Omega}}{\frac{\partial D}{\partial \lambda}}\bigg|_{\lambda = \mathrm{i}\omega_k} \right) = w_{\mathrm{HH}} \frac{\tau_{\mathrm{HH}}^2}{2\pi} \omega_k \frac{q_k (V_k + 1) - p_k W_k}{p_k^2 + q_k^2} , \end{aligned} \tag{4.27}$$

where p_k and q_k are defined by (4.11), whereas V_k and W_k are given by

$$V_k = \cos(\omega_k \tau_{\mathrm{HH}}) - 1 , \qquad W_k = -\sin(\omega_k \tau_{\mathrm{HH}}) . \tag{4.28}$$

The coefficients a_{mn} $(m,n = 1,2)$ of the cubic terms in (4.25) can be obtained from the results of center manifold reduction. These normal form coefficients can directly be calculated from the

nonlinear terms of (4.24) by applying the formulae derived in [43], whence we obtain

$$
\begin{aligned}
a_{11} =& -\frac{1}{2}w^2(V_1^2+W_1^2)\eta_2^2\left(\frac{K_1R_1+L_1S_1}{K_1^2+L_1^2}\frac{p_1V_1+q_1W_1}{p_1^2+q_1^2}+\frac{K_1S_1-L_1R_1}{K_1^2+L_1^2}\frac{q_1V_1-p_1W_1}{p_1^2+q_1^2}\right)\\
&+\frac{3}{4}w(V_1^2+W_1^2)\eta_3\frac{p_1V_1+q_1W_1}{p_1^2+q_1^2}\,,\\
a_{12} =& -w^2(V_2^2+W_2^2)\eta_2^2\left(\left(\frac{K_3R_3+L_3S_3}{K_3^2+L_3^2}+\frac{K_4R_4+L_4S_4}{K_4^2+L_4^2}\right)\frac{p_1V_1+q_1W_1}{p_1^2+q_1^2}\right.\\
&\left.+\left(\frac{K_3S_3-L_3R_3}{K_3^2+L_3^2}-\frac{K_4S_4-L_4R_4}{K_4^2+L_4^2}\right)\frac{q_1V_1-p_1W_1}{p_1^2+q_1^2}\right)+\frac{3}{2}w(V_2^2+W_2^2)\eta_3\frac{p_1V_1+q_1W_1}{p_1^2+q_1^2}\,,
\end{aligned}
\tag{4.29}
$$

where η_2 and η_3 are the cutting force coefficients that appear in (2.1), while the auxiliary parameters are

$$
\begin{aligned}
R_k &= 1-\cos(2\omega_k\tau_{\mathrm{HH}})\,, & S_k &= \sin(2\omega_k\tau_{\mathrm{HH}})\,,\\
R_{3,4} &= 1-\cos((\omega_2\pm\omega_1)\tau_{\mathrm{HH}})\,, & S_{3,4} &= \sin((\omega_2\pm\omega_1)\tau_{\mathrm{HH}})\,,\\
K_k &= wR_k-\left(4\omega_k^2-1\right)\,, & L_k &= wS_k+4\zeta\omega_k\,,\\
K_{3,4} &= wR_{3,4}-\left((\omega_2\pm\omega_1)^2-1\right)\,, & L_{3,4} &= wS_{3,4}+2\zeta(\omega_2\pm\omega_1)\,.
\end{aligned}
\tag{4.30}
$$

The expressions of a_{22} and a_{21} are the same as that of a_{11} and a_{12}, respectively, but the roles of ω_1 and ω_2 are interchanged. The formula of a_{22} can be obtained from that of a_{11} by replacing K_1, L_1, p_1, q_1, V_1, W_1, R_1 and S_1 with K_2, L_2, p_2, q_2, V_2, W_2, R_2 and S_2, respectively. Whereas the formula of a_{21} is the same as that of a_{12} but with p_2, q_2, V_2, W_2, V_1, and W_1 instead of p_1, q_1, V_1, W_1, V_2, and W_2, respectively, and replacing L_4, S_4 with $-L_4$, $-S_4$ (see the change of the sign when interchanging ω_1 and ω_2 in the definition (4.30) of L_4 and S_4).

The above formulae are valid for non-resonant double Hopf bifurcation, where the angular frequencies ω_1 and ω_2 are not related by small integer numbers. Note that for specific values of the damping ratio ζ, it might be possible to obtain weak resonant double Hopf bifurcations [44], but their analysis is out of scope of this paper. The formula (4.29) of a_{11} is the same as that obtained for the Poincaré-Lyapunov constant via the analysis of the single Hopf bifurcation in [11]. It is also important to note that the cubic coefficients a_{mn} $(m,n=1,2)$ are in fact functions of the bifurcation parameters w and Ω, and (4.29) gives only their constant approximation. In Sec. 5, we show a linear approximation of the cubic coefficients a_{mn} in terms of the bifurcation parameters w and Ω following [45]. The linear approximation leads to a higher-order estimation of the amplitude of the arising periodic and quasi-periodic motions.

5. Stability Charts and Bifurcation Diagrams

The analysis of the polar-form system (4.25) can be found in [17]. Accordingly, (4.25) can be further simplified by the transformation $r_1=\bar{r}_1/\sqrt{|a_{11}|}$, $r_2=\bar{r}_2/\sqrt{|a_{22}|}$:

$$
\begin{aligned}
\bar{r}_1' &= \bar{r}_1\left(\mu_1+a\bar{r}_1^2+b\bar{r}_2^2\right)\,,\\
\bar{r}_2' &= \bar{r}_2\left(\mu_2+c\bar{r}_1^2+d\bar{r}_2^2\right)\,,
\end{aligned}
\tag{5.1}
$$

where $a=a_{11}/|a_{11}|$, $b=a_{12}/|a_{22}|$, $c=a_{21}/|a_{11}|$ and $d=a_{22}/|a_{22}|$. These four parameters are important, since they determine the possible topologies in the phase portraits of the polar-form system (4.25). Simplified phase portraits can be depicted in the plane (r_1,r_2) for different values of the bifurcation parameters w and Ω. As it was shown in [17], the topology of these phase portraits depends on the signs of a, b, c, d and $A=ad-bc$. Depending on their signs, twelve different cases of unfolding (twelve sets of different topologies) can occur (see pages 399–409 in [17]). For (2.1), the Hopf bifurcation is always subcritical [11], thus $a>0$ and $d>0$ hold, which excludes some of these twelve cases. As it is shown below, two of the twelve topologies can be identified.

Table 1. The parameters of the double Hopf bifurcation points shown in Fig. 2.

j_1	j_2	ω_1	ω_2	Ω_{HH}	w_{HH}	γ_{11}	γ_{12}	γ_{21}	γ_{22}
1	2	1.0006	1.52994	1.01018	0.671754	0.005553	0.3623	0.2963	−0.6699
4	5	1.00247	1.15031	0.253092	0.164877	0.02429	1.251	0.3182	−1.530

Table 2. The cubic coefficients of the double Hopf bifurcation points shown in Fig. 2.

j_1	j_2	a_{11}	a_{12}	a_{21}	a_{22}	a	b	c	d	A
1	2	8.090×10^{-6}	0.008128	0.0002925	0.4317	1	0.01883	36.16	1	0.3193
4	5	1.460×10^{-4}	0.01560	0.002356	0.1121	1	0.1392	16.14	1	−1.248

(a) Phase Portraits and Topologies

Here we show a numerical case study for damping ratio $\zeta = 0.02$ and cutting-force coefficients $\eta_2 = 1.43059$ and $\eta_3 = 0.738487$, which are the dimensionless counterparts of actual measured cutting-force coefficients reported in [5] with feed $h_0 = 250$ μm per revolution. We found that topology Case Ia of [17] occurs at the intersection of the first and the second stability lobes, while the intersections of higher-order lobes are all associated with Case Ib of [17]. In what follows, we demonstrate the differences between the two cases.

Consider the intersection of the first ($j_1 = 1$) and the second ($j_2 = 2$) stability lobes, which is marked by a circle in Fig. 1(b) and is also shown by thick lines in more detail in Fig. 2(a). The first row of Tab. 1 presents the location $(\Omega_{\mathrm{HH}}, w_{\mathrm{HH}})$ of the intersection point, the two angular frequencies ω_1, ω_2 and the root tendencies γ_{mn} $(m, n = 1, 2)$. The cubic coefficients a_{mn} $(m, n = 1, 2)$ and parameters a, b, c, d and A are listed in the first row of Tab. 2. In this example, a, b, c, d and A are all positive, which corresponds to Case Ia in [17]. We also computed coefficients b and c numerically by DDE-BIFTOOL [40] and obtained the same results up to the displayed digits.

The corresponding phase portraits and their topologies are shown in Fig. 2(a). According to [17], six different topologies can be distinguished for Case Ia depending on the unfolding parameters μ_1 and μ_2. Correspondingly, six sectors with different topologies can be separated in the plane (Ω, w) of the bifurcation parameters. The straight lines separating these sectors are

$$\begin{aligned}
&\text{Line 1:} \quad \mu_1 = 0 && \Rightarrow \quad \hat{w} = -\frac{\gamma_{12}}{\gamma_{11}}\hat{\Omega}\,,\\
&\text{Line 2:} \quad \mu_2 = 0 && \Rightarrow \quad \hat{w} = -\frac{\gamma_{22}}{\gamma_{21}}\hat{\Omega}\,,\\
&\text{Line 3:} \quad \mu_2 = \frac{c}{a}\mu_1 && \Rightarrow \quad \hat{w} = \frac{c\gamma_{12} - a\gamma_{22}}{a\gamma_{21} - c\gamma_{11}}\hat{\Omega}\,,\\
&\text{Line 4:} \quad \mu_2 = \frac{d}{b}\mu_1 && \Rightarrow \quad \hat{w} = \frac{d\gamma_{12} - b\gamma_{22}}{b\gamma_{21} - d\gamma_{11}}\hat{\Omega}\,.
\end{aligned} \tag{5.2}$$

Note that Lines 1 and 2 are the tangents of the intersecting stability lobes at the double Hopf point (the lobes are shown by thick blue and cyan lines in Fig. 2).

Let us investigate the sectors of plane (μ_1, μ_2) by going around anti-clockwise. In Sector I ($\mu_1 > 0$, $\mu_2 > 0$), (4.25) has only a single, trivial equilibrium $(r_1, r_2) = (0, 0)$, which corresponds to the trivial equilibrium of the original time-delay system (2.1) and exists in all the six sectors. The trivial equilibrium $(0, 0)$ is a source (unstable node) in Sector I. The equilibrium undergoes a pitchfork bifurcation while crossing Line 1, which gives rise to a non-trivial equilibrium $(r_1, r_2) = \left(r_1^{\mathrm{P}}, 0\right)$, $r_1^{\mathrm{P}} \neq 0$ in Sector II ($\mu_1 < 0$, $\mu_2 > 0$). This equilibrium corresponds to a periodic solution (P_1) in the time-delay system (2.1), whereas the pitchfork bifurcation in system (4.25) corresponds to a Hopf bifurcation in the delay-differential equation (2.1). In Sector II, the equilibrium $\left(r_1^{\mathrm{P}}, 0\right)$ is a source, therefore the corresponding periodic solution P_1 is unstable, while the trivial

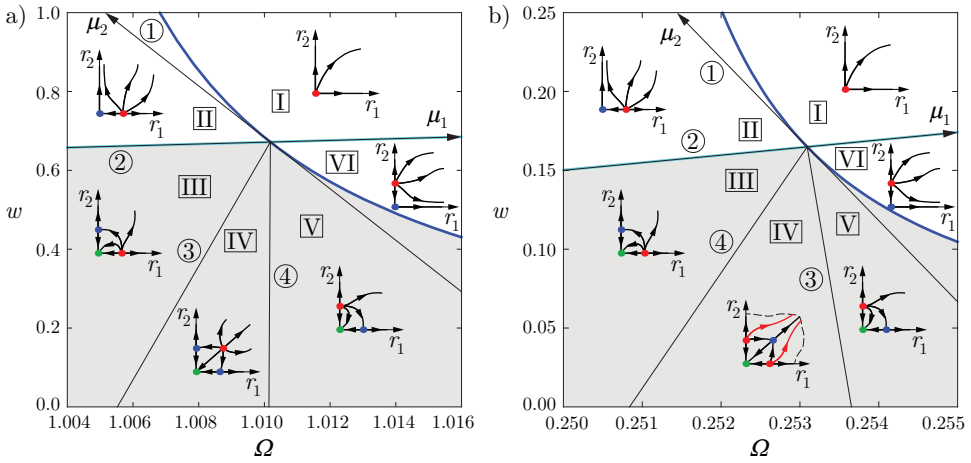

Figure 2. The possible phase portrait topologies in the vicinity of the double Hopf bifurcation at the intersection of the first and the second lobes (a); at the intersection of the fourth and the fifth lobes (b). The intersecting stability lobes are shown by thick blue and cyan lines. Sources, sinks and saddles are indicated by red, green and blue dots, respectively.

equilibrium $(0,0)$ becomes a saddle. Another pitchfork bifurcation of $(0,0)$ takes place along Line 2, and a non-trivial equilibrium $(r_1,r_2)=\left(0,r_2^{\mathrm{p}}\right)$, $r_2^{\mathrm{p}}\neq 0$ is born when entering Sector III ($\mu_1<0$, $c\mu_1/a<\mu_2<0$). This, again, corresponds to a Hopf bifurcation of the equilibrium of the infinite-dimensional time-delay system (2.1), which gives rise to another periodic solution (P_2). In Sector III, the trivial equilibrium becomes a sink (stable node), the equilibrium $\left(r_1^{\mathrm{p}},0\right)$ remains a source and the equilibrium $\left(0,r_2^{\mathrm{p}}\right)$ is a saddle. When entering Sector IV ($\mu_1<0$, $d\mu_1/b<\mu_2<c\mu_1/a$), a pitchfork bifurcation of $\left(r_1^{\mathrm{p}},0\right)$ gives rise to the non-trivial equilibrium $(r_1,r_2)=\left(r_1^{\mathrm{qp}},r_2^{\mathrm{qp}}\right)$, $r_1^{\mathrm{qp}}\neq 0$, $r_2^{\mathrm{qp}}\neq 0$. This phenomenon corresponds to a torus bifurcation of the periodic solution P_1 of (2.1), by which a quasi-periodic solution (QP) arises. Thus, in Sector IV, the trivial equilibrium coexists with two periodic solutions and a quasi-periodic one. The trivial equilibrium is still a sink, the equilibrium $\left(0,r_2^{\mathrm{p}}\right)$ is still a saddle, while the equilibrium $\left(r_1^{\mathrm{p}},0\right)$ becomes a saddle and the equilibrium $\left(r_1^{\mathrm{qp}},r_2^{\mathrm{qp}}\right)$ is born as a source. The equilibrium $\left(r_1^{\mathrm{qp}},r_2^{\mathrm{qp}}\right)$ merges with the equilibrium $\left(0,r_2^{\mathrm{p}}\right)$ via a pitchfork bifurcation when leaving Sector IV by crossing Line 4 to Sector V ($\mu_1<0$, $\mu_2<d\mu_1/b$). Equivalently, a torus bifurcation of P_2 occurs in the infinite-dimensional system (2.1). In Sector V, the equilibrium $\left(0,r_2^{\mathrm{p}}\right)$ becomes a source, while the equilibrium $\left(r_1^{\mathrm{p}},0\right)$ remains a saddle and the trivial equilibrium remains a sink. Entering Sector VI ($\mu_1>0$, $\mu_2<0$) by crossing Line 1, the equilibrium $\left(r_1^{\mathrm{p}},0\right)$ disappears via a pitchfork bifurcation, which corresponds to a Hopf bifurcation of the trivial equilibrium of (2.1). Here, the equilibrium $\left(0,r_2^{\mathrm{p}}\right)$ remains a source and the trivial equilibrium becomes a saddle. Finally, the equilibrium $\left(r_2^{\mathrm{p}},0\right)$ disappears via a pitchfork bifurcation when returning to Sector I by crossing Line 2, i.e., P_2 vanishes as a result of a Hopf bifurcation in the time-delay system (2.1).

A second example is presented in Fig. 2(b), where the intersection of the fourth ($j_1=4$) and the fifth ($j_2=5$) stability lobes is shown, see also the square mark in Fig. 1(b). The parameters of the double Hopf point, the corresponding root tendencies and the cubic coefficients are listed in the second row of Tab. 1 and Tab. 2. In this example, a, b, c and d are positive but now A is negative, thus Case Ib in [17] applies. In this case, the order of Lines 3 and 4 changes when going around the sectors of the plane (μ_1,μ_2) anti-clockwise. Therefore, the quasi-periodic solution QP is born from P_2 (and not P_1) when entering Sector IV along Line 4, and it collapses into P_1 (and not P_2) when leaving Sector IV along Line 3. Interchanging Lines 3 and 4 modifies the topology only in Sector IV: now the equilibria $\left(r_1^{\mathrm{p}},0\right)$ and $\left(0,r_2^{\mathrm{p}}\right)$ are sources and the equilibrium $\left(r_1^{\mathrm{qp}},r_2^{\mathrm{qp}}\right)$ is a saddle. Consequently, the periodic solutions P_1 and P_2 behave as sources and the quasi-periodic solution QP behaves as a saddle.

(b) Bifurcation Diagrams via Higher-Order Estimation

The amplitudes of the arising periodic and quasi-periodic orbits can be determined by calculating the non-trivial equilibria of (5.1). According to [17], they can be calculated as

$$\begin{aligned}
\mathrm{P}_1: \quad & \bar{r}_1^{\mathrm{p}} = \sqrt{-\frac{\mu_1}{a}} && \Rightarrow \quad r_1^{\mathrm{p}}(\hat{w},\hat{\Omega}) = \sqrt{-\frac{\gamma_{11}\hat{w}+\gamma_{12}\hat{\Omega}}{a_{11}}}\,, \\
\mathrm{P}_2: \quad & \bar{r}_2^{\mathrm{p}} = \sqrt{-\frac{\mu_2}{d}} && \Rightarrow \quad r_2^{\mathrm{p}}(\hat{w},\hat{\Omega}) = \sqrt{-\frac{\gamma_{21}\hat{w}+\gamma_{22}\hat{\Omega}}{a_{22}}}\,, \\
\mathrm{QP}: \quad & \bar{r}_1^{\mathrm{qp}} = \sqrt{\frac{b\mu_2 - d\mu_1}{A}} && \Rightarrow \quad r_1^{\mathrm{qp}}(\hat{w},\hat{\Omega}) = \sqrt{\frac{(a_{12}\gamma_{21}-a_{22}\gamma_{11})\,\hat{w}+(a_{12}\gamma_{22}-a_{22}\gamma_{12})\,\hat{\Omega}}{a_{11}a_{22}-a_{12}a_{21}}}\,, \\
& \bar{r}_2^{\mathrm{qp}} = \sqrt{\frac{c\mu_1 - a\mu_2}{A}} && \Rightarrow \quad r_2^{\mathrm{qp}}(\hat{w},\hat{\Omega}) = \sqrt{\frac{(a_{21}\gamma_{11}-a_{11}\gamma_{21})\,\hat{w}+(a_{21}\gamma_{12}-a_{11}\gamma_{22})\,\hat{\Omega}}{a_{11}a_{22}-a_{12}a_{21}}}\,.
\end{aligned} \tag{5.3}$$

Here we emphasise that the amplitudes depend on the two bifurcation parameters $\hat{w}$ and $\hat{\Omega}$. Later on we omit the argument $(\hat{w},\hat{\Omega})$ for simplicity.

In [45], it was show that a higher-order estimation of the amplitude of the periodic orbits arising from Hopf bifurcation is possible when special global properties hold in the system. This estimation can also be done for the quasi-periodic orbit arising from the double Hopf bifurcation. The estimation is based on the approximation of the cubic coefficients a_{mn} $(m,n=1,2)$ by a linear function of the bifurcation parameters Ω, w instead of using the constant values defined by (4.29):

$$\hat{a}_{mn} = a_{mn} + a_{mn}^{\Omega}\hat{\Omega} + a_{mn}^{w}\hat{w}\,, \tag{5.4}$$

$m,n=1,2$. Replacing a_{mn} with $\hat{a}_{mn}$ in (5.3) yields a higher-order estimation of the amplitude of the periodic and the quasi-periodic orbits as long as the additional coefficients a_{mn}^{Ω} and a_{mn}^{w} are chosen properly.

The additional coefficients can be calculated based on the following global properties of the system. When the chip width is zero, that is, $w=0$, the cutting force on the right-hand side of the governing equation (2.1) vanishes and the system reduces to a damped free oscillator. Hence the periodic and the quasi-periodic solutions must disappear at $w=0$, which happens such that their amplitudes tend to infinity. That is, $\lim_{w\to 0} r_1^{\mathrm{p}} = \infty$ and $\lim_{w\to 0} r_2^{\mathrm{p}} = \infty$ holds for the periodic solutions, whereas $\lim_{w\to 0} r_1^{\mathrm{qp}} = \infty$ and $\lim_{w\to 0} r_2^{\mathrm{qp}} = \infty$ for the quasi-periodic solution. Similarly, when $\tau = 0$ or, equivalently, $\Omega \to \infty$, the right-hand side of (2.1) becomes zero. Therefore, the periodic solutions satisfy $\lim_{\Omega\to\infty} r_1^{\mathrm{p}} = \infty$ and $\lim_{\Omega\to\infty} r_2^{\mathrm{p}} = \infty$, whereas the quasi-periodic solution satisfies $\lim_{\Omega\to\infty} r_1^{\mathrm{qp}} = \infty$ and $\lim_{\Omega\to\infty} r_2^{\mathrm{qp}} = \infty$. It can be shown that these properties are guaranteed with the coefficients

$$\hat{a}_{mn} = a_{mn} + \frac{a_{mn}}{w_{\mathrm{HH}}}\hat{w}\,, \tag{5.5}$$

$m,n=1,2$. Note that approximating the cubic coefficients by such linear functions of the bifurcation parameters instead of using the constants in (4.29) does not change the formulae of Lines 1-4 in (5.2).

The periodic and quasi-periodic solutions of (2.1) can be approximated as

$$\begin{aligned}
\mathbf{y}_t(\theta) \approx & r_1(\hat{w},\hat{\Omega})\left(\cos(\omega_1 t)\mathbf{s}_{1,\mathrm{R}}(\theta) - \sin(\omega_1 t)\mathbf{s}_{1,\mathrm{I}}(\theta)\right) \\
& + r_2(\hat{w},\hat{\Omega})\left(\cos(\omega_2 t)\mathbf{s}_{2,\mathrm{R}}(\theta) - \sin(\omega_2 t)\mathbf{s}_{2,\mathrm{I}}(\theta)\right)\,,
\end{aligned} \tag{5.6}$$

$$x(t) = y_{t1}(0) \approx r_1(\hat{w},\hat{\Omega})\cos(\omega_1 t) + r_2(\hat{w},\hat{\Omega})\cos(\omega_2 t)\,, \tag{5.7}$$

where $(r_1,r_2) = (r_1^{\mathrm{p}},0)$ and $(r_1,r_2) = (0,r_2^{\mathrm{p}})$ must be substituted for the periodic solutions P_1 and P_2, respectively, whereas $(r_1,r_2) = (r_1^{\mathrm{qp}},r_2^{\mathrm{qp}})$ for the quasi-periodic solution QP with the amplitudes given by (5.3) using $\hat{a}_{mn}$ instead of a_{mn}. The bifurcation diagrams presenting the

amplitude of the periodic and the quasi-periodic solutions will be presented in Fig. 3 together with the corresponding global stability charts.

(c) Global Dynamics and Region of Bistability

In the linearly stable region, where the equilibrium is a sink, the coexisting periodic and quasi-periodic solutions are unstable. Due to these unstable orbits, the basin of attraction of the linearly stable equilibrium is finite, hence the equilibrium is not stable in the global sense. To large enough perturbations, the vibrations of the machine tool amplify in a self-excited manner.

When the vibration amplitude becomes large enough, the tool jumps out of the workpiece and leaves the material during cutting. In such cases, the tool's motion is governed by non-smooth dynamics: switching occurs between the dynamics of a cutting tool and the dynamics of a 'flying' tool (a damped free oscillator). The switching surface is located where the chip thickness is zero and loss of contact takes place. If the tool loses contact with the workpiece and undergoes a free flight, then (2.1) becomes no longer valid, since the cutting force on the right-hand side vanishes. It was shown in [14] for the case of the single Hopf bifurcation that once the unstable periodic motion involves loss of contact and grazes the switching surface, the periodic orbit undergoes a kind of non-smooth fold of limit cycles bifurcation called Big Bang Bifurcation (B^3). This bifurcation is illustrated in Fig. 1(c) for $j=2$, $\omega=1.37$ ($\Omega=0.901$) as shown by the dashed line in Fig. 1(b). Via the non-smooth fold, the unstable periodic orbit vanishes by merging with a large-amplitude attractive solution. This solution describes machine tool chatter with intermittent loss of contact, it may be chaotic and it coexists with the unstable periodic orbit and the linearly stable equilibrium. The region of coexistence is also called unsafe zone or region of bistability. Determining the boundary of the bistable region is important, since the cutting process unsafe in this region: it is stable only linearly but not in the global sense.

We can expect similar behaviour in the vicinity of the double Hopf point. Periodic and quasi-periodic solutions exist only up to the point where the tool first loses contact with the workpiece during its large-amplitude motion. Thus, a Big Bang Bifurcation happens where the dimensionless chip thickness $h(t)$ first drops to zero, that is, when

$$h(t)=1+x(t-\tau)-x(t)=0 \tag{5.8}$$

occurs for any t. Equation (5.8) defines the loci of the Big Bang Bifurcation and gives the boundary of the bistable region for the periodic and the quasi-periodic solutions. Substituting (5.7) into (5.8), combining the trigonometric terms and approximating $\tau\approx\tau_{\mathrm{HH}}$, we get

$$r_1(\hat{w},\hat{\Omega})\sqrt{\left(1-\cos(\omega_1\tau_{\mathrm{HH}})\right)^2+\sin^2(\omega_1\tau_{\mathrm{HH}})}\cos\left(\omega_1 t+\phi_1\right) + r_2(\hat{w},\hat{\Omega})\sqrt{\left(1-\cos(\omega_2\tau_{\mathrm{HH}})\right)^2+\sin^2(\omega_2\tau_{\mathrm{HH}})}\cos\left(\omega_2 t+\phi_2\right)=1\,, \tag{5.9}$$

where ϕ_1 and ϕ_2 are certain phase shifts. If there exists any t for which (5.9) holds, then loss of contact takes place and the periodic or the quasi-periodic solutions disappear. The smallest amplitude for which loss of contact might occur is obtained by substituting $\cos\left(\omega_1 t+\phi_1\right)=1$ and $\cos\left(\omega_2 t+\phi_2\right)=1$. This motivates the introduction of the scaled amplitude

$$r:=r_1(\hat{w},\hat{\Omega})\sqrt{2\left(1-\cos(\omega_1\tau_{\mathrm{HH}})\right)}+r_2(\hat{w},\hat{\Omega})\sqrt{2\left(1-\cos(\omega_2\tau_{\mathrm{HH}})\right)} \tag{5.10}$$

and $r=1$ indicates loss of contact. If $r>1$, then the periodic and the quasi-periodic solutions disappear via the Big Bang Bifurcation. Note that the quasi-periodic solution is located on an invariant torus. Taking $\cos\left(\omega_1 t+\phi_1\right)=1$ and $\cos\left(\omega_2 t+\phi_2\right)=1$ implies that the solution is assumed to be dense where the torus touches the switching surface (5.8).

Taking $r=1$, substituting the higher-order estimation of the amplitude of the periodic solutions given by (5.3) with $\hat{a}_{mn}$ instead of a_{mn}, we can obtain the boundary where the periodic

solutions disappear via a Big Bang Bifurcation in the form

$$\hat{w}^{\mathrm{B}^3}_{\mathrm{P}_k}(\hat{\Omega}) = -\frac{\gamma_{k2}\hat{\Omega} + \dfrac{a_{kk}}{2\left(1-\cos(\omega_k \tau_{\mathrm{HH}})\right)}}{\gamma_{k1} + \dfrac{a_{kk}}{2w_{\mathrm{HH}}\left(1-\cos(\omega_k \tau_{\mathrm{HH}})\right)}}\,. \tag{5.11}$$

The boundary $\hat{w}^{\mathrm{B}^3}_{\mathrm{QP}}(\hat{\Omega})$ where the quasi-periodic solution vanishes can be determined the same way by symbolic algebra (the resulting formula is too long to be presented here). If any of the unstable periodic or quasi-periodic solutions exists, a large-amplitude attractive solution coexists with the stable equilibrium. Therefore, the boundary of the bistable region is determined by those Big Bang Bifurcation curves, which are the farthest from the linear stability boundary.

The results are summarised in Fig. 3 where the double Hopf points (DH) at the intersections of the first and the second, the second and the third, and the fourth and the fifth lobes are considered in rows (a), (b) and (c), respectively. In each panel, the analytical results are indicated by solid lines. The left panels show the stability charts of the system. The right panels show the corresponding bifurcation diagrams with the amplitude r of the periodic orbits P_1, P_2 and the quasi-periodic orbit QP as a function of the bifurcation parameter w. Parameter Ω is fixed to $\Omega = 1.0095$, $\Omega = 0.505$ and $\Omega = 0.2527$ in rows (a), (b) and (c), respectively, which correspond to the dotted vertical lines in the left panels. In the left panels, solid thick blue and cyan lines show the intersecting stability lobes given by (3.3), whereas their tangents (Lines 1 and 2) are indicated by thin blue and cyan lines. Note that in the region depicted, Line 2 overlaps with the solid thick cyan stability lobe. In the right panels, the periodic orbits P_1 and P_2 initiate from the (approximate) Hopf bifurcation points $\mathrm{H}(\mathrm{P}_1)$ and $\mathrm{H}(\mathrm{P}_2)$, which correspond to the intersections of the dotted line with Lines 1 and 2 in the left panels of Fig. 3, respectively. The periodic orbits undergo a torus bifurcation along the red and purple lines (Lines 3 and 4) in the left panels. In the right panel of Fig. 3(a), the quasi-periodic solution QP is born from the periodic solution P_1 through a torus bifurcation at $\mathrm{T}(\mathrm{P}_1)$, which corresponds to the intersection of the dotted line and Line 3 in the left panel. In Figs. 3(b) and 3(c), the quasi-periodic orbit QP arises from the other periodic solution P_2 through a torus bifurcation at $\mathrm{T}(\mathrm{P}_2)$, see also the intersection of the dotted line and Line 4 in the left panels.

The bifurcation diagrams in the right panels of Fig. 3 are valid only up to points $\mathrm{B}^3(\mathrm{P}_1)$, $\mathrm{B}^3(\mathrm{P}_2)$ and $\mathrm{B}^3(\mathrm{QP})$ at $r = 1$, where (2.1) becomes invalid due to loss of contact between the tool and the workpiece. The branches are invalid for $r > 1$, the periodic and the quasi-periodic solutions vanish there and large-amplitude stable solutions are born via a non-smooth fold. In the left panels, solid green and orange lines show the loci of Big Bang Bifurcation given by (5.11) for the periodic orbits P_1 and P_2, respectively. The Big Bang Bifurcation curve for the quasi-periodic solution is shown by a black line. Dark gray shading shows the regions where the periodic orbits indeed exist, that is, without losing contact with the workpiece. Similarly, darker gray shading indicates the region where the quasi-periodic solution exists. Light gray shading indicates the region where no periodic or quasi-periodic orbits exist due to loss of contact. Only the stable equilibrium exists here, hence the system is globally stable. In the regions with dark gray and darker gray shading, the system is bistable. Based on the figure, the quasi-periodic orbit occurs in a narrow range of parameters and does not affect the boundary of the globally stable region. Consequently, even close to the intersection of the stability lobes, the globally stable region can be determined by the formulas obtained from the analysis of the single Hopf bifurcation [11].

We calculated the amplitude of solutions by numerical continuation as well, see the dashed lines in Fig. 3. We used DDE-BIFTOOL [40] for the computation of the periodic orbits, and used the algorithm in [15,41] to compute the quasi-periodic orbit. The loci of torus and Big Bang Bifurcations have also been continued in two parameters, see the dashed lines in the left panels. Note that the analytical results are only approximations and the numerical results can be considered as exact ones. We can see that the analytical results give only the tangents of the numerical torus bifurcation branches. The agreement between the analytical and numerical results is better in the right panels of Figs. 3(b) and 3(c) than in Fig. 3(a). At the intersection of the

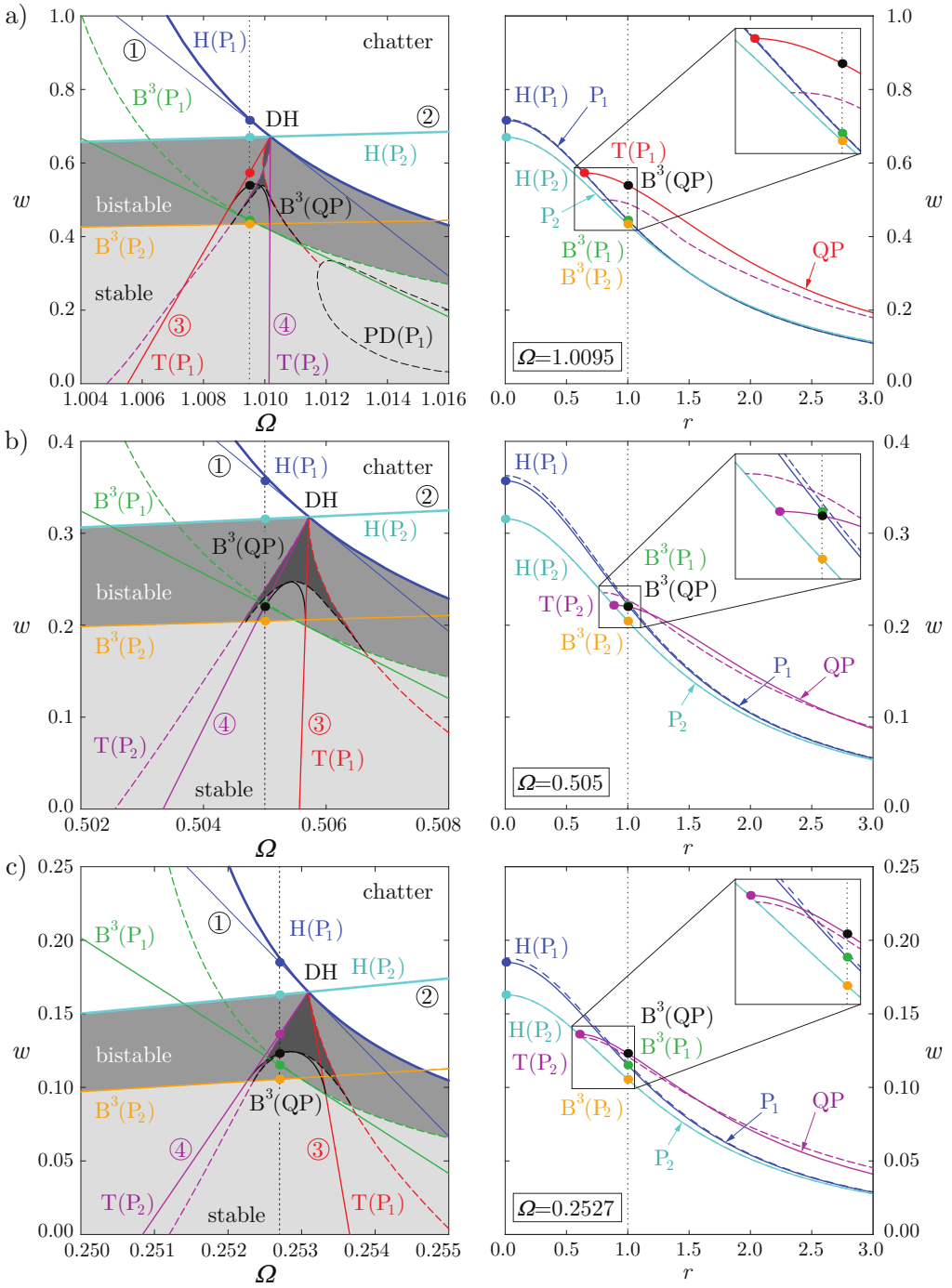

Figure 3. Stability charts (left) and bifurcation diagrams (right) close to the double Hopf point (DH) at the intersection of the first and the second lobe (a); the second and the third lobe (b); the fourth and the fifth lobe (c). Analytical results are indicated by solid lines and dashed lines show the numerical results. Blue and cyan lines show the loci of Hopf bifurcation (H) where periodic solutions (P_1 and P_2) are born. Red and purple lines represent the loci of torus bifurcation (T) where a quasi-periodic orbit (QP) emerges from one of the periodic orbits. Green, orange and black lines indicate the loci of Big Bang Bifurcation (B^3) where the tool loses contact with the workpiece during periodic or quasi-periodic oscillations. Thin black line indicates period doubling bifurcation (PD). The globally stable region is indicated by light gray shading, whereas dark gray and darker gray shadings show the bistable regions where unstable periodic and quasi-periodic solutions coexist with the linearly stable equilibrium and the large-amplitude stable motion (chatter) that involves loss of contact.

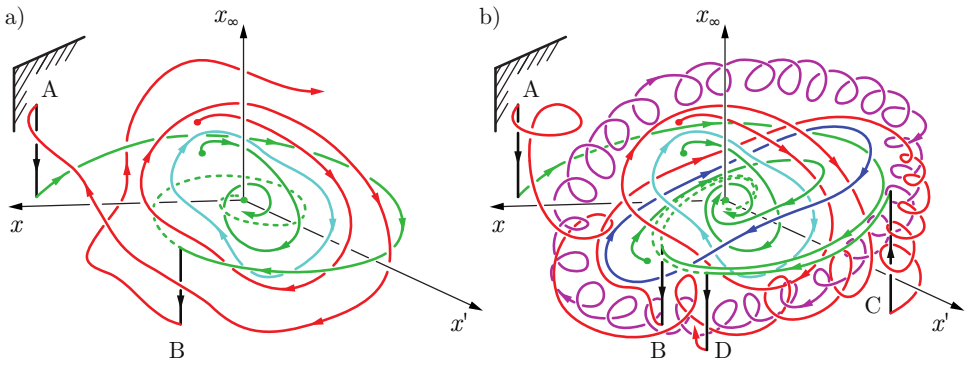

Figure 4. Trajectories of the cutting process in the neighbourhood of a single periodic orbit (a); trajectories where two periodic orbits coexist with a quasi-periodic one (b).

first and the second stability lobes in Fig. 3(a), the analytical results for the torus bifurcation curves are valid only in the close vicinity of the double Hopf point, then the numerical branches deviate. Therefore, the analytical bifurcation diagram in the right panel is not accurate even qualitatively: the quasi-periodic solution is born from the other periodic solution as in the numerical case. The numerical counterparts of the Big Bang Bifurcation branches $\mathrm{B}^3(\mathrm{P}_1)$ and $\mathrm{B}^3(\mathrm{P}_2)$ are also shown by dashed green and orange lines in the left panels of Fig. 3. Again, the analytical results give only the tangents of the numerical branches. Note that the solid and dashed orange lines overlap. The dashed green and orange lines can also be obtained by analytical formulae using the results of [11,45] on the single Hopf bifurcation, which considers the entire stability lobes not only their intersection. In addition, numerical continuation showed that even a period doubling bifurcation of the periodic solution P_1 can occur, see the dashed thin black line $\mathrm{PD}(\mathrm{P}_1)$ in the left panel of Fig. 3(a). However, this branch lies beyond the Big Bang Bifurcation $\mathrm{B}^3(\mathrm{P}_1)$, hence the period doubling does not show up when considering loss of contact between the tool and the workpiece.

Finally, Fig. 4 shows a qualitative picture about the trajectories of the infinite-dimensional non-smooth system including loss of contact between the tool and the workpiece. The infinite-dimensional phase space is illustrated by three axes: x and x', which are the general coordinates of the corresponding delay-free system, and x_∞, which is introduced only for illustration purposes to represent the other infinitely many dimensions as a cumulative effect of the past. Panel (a) shows the case where only a single periodic orbit (cyan line) exists in the vicinity of the equilibrium. Here, the trajectories which lie within the basin of attraction of the equilibrium tend towards the equilibrium, see the solely green trajectory. However, the basin of attraction is finite and trajectories lying outside spiral outwards, see the red line. In this case, the vibrations amplify until the trajectory hits the switching surface (5.8) indicated by hatches at point A. Here, the tool jumps out of the workpiece. When the tool is out of contact, the infinite-dimensional system reduces to a two-dimensional one as shown by the black line. Temporarily, the system behaves as a damped free oscillator, which is illustrated by the trajectories spiralling towards the origin in the plane (x, x') (see the green line). The amplitude of the vibrations decreases until the tool gets back into the workpiece at point B. The system becomes infinite-dimensional again (black line) and the trajectory diverges from the origin again (red line).

Figure 4(b) shows the case where two periodic solutions (blue and cyan lines) and a quasi-periodic solution (purple line) coexist, cf. Sector IV in Fig. 2. The green trajectories lie within the basin of attraction of the equilibrium, hence they spiral towards the origin. The red trajectory lies outside and diverges from the origin. Note that this red trajectory is only a possible example, and it can be considered as the representation of the red lines in Sector IV of Fig. 2(b). The solution initiates in the vicinity of one periodic solution, cf. the upper red curve in Fig. 2(b). The trajectory spirals outwards, wraps around the quasi-periodic solution, and runs until it hits the switching

surface (5.8) at point A, see the hatches in Fig. 4(b) and the dashed line in Fig. 2(b). Here, the tool gets out of the workpiece (black line), the system becomes two-dimensional and restricted to plane (x, x'), where the trajectory spirals towards the origin (green line). Then, the tool enters the workpiece at point B (black line) and the solution continues in the vicinity of the other periodic orbit (red line), cf. the lower red curve in Fig. 2(b). The vibrations start amplifying again until the contact between the tool and the workpiece is lost at point C (black line). A damped motion (green line) follows in the plane (x, x') until point D is reached. The tool gets back into the workpiece again (black line) and, once more, the infinite-dimensional dynamics prevails. The whole trajectory may even describe chaotic motion. The chaos can be transient, since it can occur that, after a while, the trajectory penetrates the basin of attraction of the equilibrium when the tool gets back into the workpiece. Then, at last, the system becomes globally stable and the trajectory approaches the origin.

6. Conclusions

In this paper, we investigated the dynamics of machine tool vibrations in the vicinity of a double Hopf bifurcation point. Via center manifold reduction, we derived the normal form coefficients of the four-dimensional center subsystem, which determines the long-term dynamics in the vicinity of the double Hopf point. Based on the normal form coefficients, we identified the possible topologies in the phase space of the four-dimensional center subsystem. We found the previously unexplored Case Ia of [17] and also the Case Ib that was predicted in [27], and showed that unstable periodic and quasi-periodic solutions coexist with the linearly stable equilibrium in certain parameter regions. Taking loss of contact between the tool and the workpiece into account, we derived the approximate boundaries of the globally stable region in closed form. We verified the results by numerical continuation using DDE-BIFTOOL [40] and the algorithm of [15,41], which even revealed the existence of period doubling bifurcation of periodic orbits. Finally, we assessed qualitatively the non-smooth global dynamics in the infinite-dimensional phase space and pointed out the possibility of transient chaotic motions.

Ethics. This work did not involve any research on humans or animals.

Data Accessibility. This work does not have any experimental data.

Authors' Contributions. Tamas G. Molnar was responsible for the analytical bifurcation analysis, Zoltan Dombovari carried out the numerical continuation. Gabor Stepan and Tamas Insperger supervised the project. All authors contributed to writing the paper and gave final approval for publication.

Competing Interests. We declare we have no competing interests.

Funding. This work has been supported by the ÚNKP-16-3-I. New National Excellence Program of the Ministry of Human Capacities. This work has received funding from the János Bolyai Research Scholarship of MTA (BO/00589/13/6). The research leading to these results has received funding from the European Research Council under the European Union's Seventh Framework Programme (FP/2007-2013) / ERC Advanced Grant Agreement n. 340889.

References

1. S. A. Tobias, W. Fishwick, Theory of regenerative machine tool chatter, The Engineer (1958) 199–203, 238–239.
2. J. Tlusty, M. Polacek, The stability of the machine tool against self-excited vibration in machining, in: ASME Production Engineering Research Conference, Pittsburgh, 1963, pp. 454–465.
3. J. Hale, Theory of Functional Differential Equations, Springer, New York, 1977.
4. G. Stépán, Z. Dombóvári, J. Muñoa, Identification of cutting force characteristics based on chatter experiments, CIRP Annals - Manufacturing Technology 60 (1) (2011) 113–116.
5. H. M. Shi, S. A. Tobias, Theory of finite amplitude machine tool instability, International Journal of Machine Tool Design and Research 24 (1) (1984) 45–69.

6. W. J. Endres, M. Loo, Modeling cutting process nonlinearity for stability analysis - application to tooling selection for valve-seat machining, in: 5th CIRP International Workshop on Modeling of Machining, West Lafayette, IN, USA, 2002, pp. 71–82.
7. N. K. Chandiramani, T. Pothala, Dynamics of 2-dof regenerative chatter during turning, Journal of Sound and Vibration 290 (1–2) (2006) 448–464.
8. K. Ahmadi, F. Ismail, Experimental investigation of process damping nonlinearity in machining chatter, International Journal of Machine Tools and Manufacture 50 (11) (2010) 1006–1014.
9. G. Stépán, T. Kalmár-Nagy, Nonlinear regenerative machine tool vibrations, in: Proceedings of DETC'97, ASME Design and Technical Conferences, Sacramento, CA, USA, 1997, pp. 1–11.
10. T. Kalmár-Nagy, G. Stépán, F. C. Moon, Subcritical Hopf bifurcation in the delay equation model for machine tool vibrations, Nonlinear Dynamics 26 (2001) 121–142.
11. Z. Dombóvári, R. E. Wilson, G. Stépán, Estimates of the bistable region in metal cutting, Proceedings of the Royal Society A - Mathematical, Physical and Engineering Sciences 464 (2008) 3255–3271.
12. A. H. Nayfeh, Order reduction of retarded nonlinear systems – the method of multiple scales versus center-manifold reduction, Nonlinear Dynamics 51 (4) (2008) 483–500.
13. K. Nandakumar, P. Wahi, A. Chatterjee, Infinite dimensional slow modulations in a well known delayed model for cutting tool vibrations, Nonlinear Dynamics 62 (4) (2010) 705–716.
14. Z. Dombóvári, D. A. Barton, R. E. Wilson, G. Stépán, On the global dynamics of chatter in the orthogonal cutting model, International Journal of Non-Linear Mechanics 46 (1) (2011) 330–338.
15. Z. Dombóvári, G. Stépán, On the bistable zone of milling processes, Philosophical Transactions of the Royal Society A: Mathematical, Physical and Engineering Sciences 373 (2015) 20140409.
16. B. D. Hassard, N. D. Kazarinoff, Y.-H. Wan, Theory and Applications of Hopf Bifurcation, London Mathematical Society Lecture Note Series **41**, Cambridge, 1981.
17. J. Guckenheimer, P. Holmes, Nonlinear Oscillations, Dynamical Systems, and Bifurcations of Vector Fields, Springer, New York, 1983.
18. G. Stépán, Retarded dynamical systems, Longman, Harlow, 1989.
19. Y. A. Kuznetsov, Elements of Applied Bifurcation Theory, Springer, New York, 1998.
20. S. A. Campbell, Calculating centre manifolds for delay differential equations using maple, in: B. Balachandran, T. Kalmar-Nagy, D. E. Gilsinn (Eds.), Delay Differential Equations, Springer, New York, 2009, pp. 221–244.
21. A. H. Nayfeh, D. T. Mook, Nonlinear Oscillations, Wiley, New York, 1979.
22. J. Hale, Averaging methods for differential equations with retarded arguments and a small parameter, Journal of Differential Equations 2 (1) (1966) 57–73.
23. J. Hale, S. M. V. Lunel, Averaging in infinite dimensions, Journal of Integral Equations and Applications 2 (4) (1990) 463–494.
24. B. Lehman, S. P. Weibel, Fundamental theorems of averaging for functional differential equations, Journal of Differential Equations 152 (1) (1999) 160–190.
25. J. A. Sanders, F. Verhulst, J. Murdock, Averaging Methods in Nonlinear Dynamical Systems, Springer, New York, 2007.
26. T. Sari, Averaging for ordinary differential equations and functional differential equations, in: I. van den Berg, V. Neves (Eds.), The Strength of Nonstandard Analysis, Springer, Wien, 2007, pp. 286–305.
27. G. Stépán, Modelling nonlinear regenerative effects in metal cutting, Philosophical Transactions of the Royal Society A: Mathematical, Physical and Engineering Sciences 359 (1781) (2001) 739–757.
28. S. A. Campbell, J. Bélair, T. Ohira, J. Milton, Limit cycles, tori, and complex dynamics in a second-order differential equation with delayed negative feedback, Journal of Dynamics and Differential Equations 7 (1) (1995) 213–236.
29. G. Stépán, G. Haller, Quasiperiodic oscillations in robot dynamics, Nonlinear Dynamics 8 (4) (1995) 513–528.
30. S. A. Campbell, V. G. LeBlanc, Resonant Hopf-Hopf interactions in delay differential equations, Journal of Dynamics and Differential Equations 10 (2) (1998) 327–346.
31. J. Xu, K.-W. Chung, C.-L. Chan, An efficient method for studying weak resonant double Hopf bifurcation in nonlinear systems with delayed feedbacks, SIAM Journal on Applied Dynamical Systems 6 (1) (2007) 29–60.

32. S. Guo, Y. Chen, J. Wu, Two-parameter bifurcations in a network of two neurons with multiple delays, Journal of Differential Equations 244 (2) (2008) 444–486.
33. S. Ma, Q. Lu, Z. Feng, Double Hopf bifurcation for Van der Pol-Duffing oscillator with parametric delay feedback control, Journal of Mathematical Analysis and Applications 338 (2) (2008) 993–1007.
34. W. Wang, J. Xu, Multiple scales analysis for double Hopf bifurcation with 1:3 resonance, Nonlinear Dynamics 66 (1) (2011) 39–51.
35. C. Bazsó, A. R. Champneys, C. J. Hős, Bifurcation analysis of a simplified model of a pressure relief valve attached to a pipe, SIAM Journal on Applied Dynamical Systems 13 (2) (2014) 704–721.
36. R. Qesmi, M. A. Babram, Double Hopf bifurcation in delay differential equations, Arab Journal of Mathematical Sciences 20 (2) (2014) 280–301.
37. Z. Shen, C. Zhang, Double Hopf bifurcation of coupled dissipative Stuart-Landau oscillators with delay, Applied Mathematics and Computation 227 (2014) 553–566.
38. Y. Ding, J. Cao, W. Jiang, Double Hopf bifurcation in active control system with delayed feedback: application to glue dosing processes for particleboard, Nonlinear Dynamics 83 (3) (2016) 1567–1576.
39. P. Wahi, A. Chatterjee, Regenerative tool chatter near a codimension 2 Hopf point using multiple scales, Nonlinear Dynamics 40 (4) (2005) 323–338.
40. K. Engelborghs, T. Luzyanina, D. Roose, Numerical bifurcation analysis of delay differential equations using DDE-BIFTOOL, ACM Transactions on Mathematical Software 28 (1) (2002) 1–21.
41. D. Roose, R. Szalai, Continuation and bifurcation analysis of delay differential equations, in: B. Krauskopf, H. M. Osinga, J. Galán-Vioque (Eds.), Numerical continuation methods for dynamical systems: Path following and boundary value problems, Springer Netherlands, 2007, pp. 359–399.
42. R. Szalai, Knut: A continuation and bifurcation software for delay-differential equations, http://rs1909.github.io/knut/ (2005-2013).
43. E. Knobloch, Normal form coefficients for the nonresonant double Hopf bifurcation, Physics Letters A 116 (8) (1986) 365–369.
44. W. Wang, J. Xu, X. Sun, Strong and weak resonances in delayed differential systems, International Journal of Bifurcation and Chaos 23 (7) (2013) 1350119.
45. T. G. Molnár, T. Insperger, G. Stépán, Analytical estimations of limit cycle amplitude for delay-differential equations, Electronic Journal of Qualitative Theory of Differential Equations 2016 (77) (2016) 1–10.